This is a repository copy of *NO emission and enhanced thermal performances studies on counter-flow double-channel hydrogen/ammonia-fuelled microcombustors with oval-shaped internal threads*.

White Rose Research Online URL for this paper:
https://eprints.whiterose.ac.uk/196653/

Version: Published Version
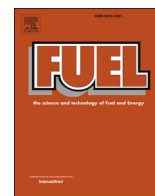
Full Length Article

NO emission and enhanced thermal performances studies on Counter-flow Double-channel Hydrogen/Ammonia-fuelled microcombustors with Oval-shaped internal threads

He Zhao [a], Dan Zhao [a],[*], Sid Becker [a], Yang Zhang [b]

[a] *Department of Mechanical Engineering, University of Canterbury, Private Bag 4800, Christchurch 8041, New Zealand*
[b] *Department of Mechanical Engineering, University of Sheffield, Sheffield, UK*

A B S T R A C T

Micro-combustion systems play a critical role in powering microreactors, micropropulsion and other micro-energy conversion systems. In this work, we have numerically investigated a double-channel counter-flow micro-combustor fuelled by premixed ammonia/hydrogen/oxygen parametric to investigate both NO emissions and thermal performance. The model is used to examine the effects of 1) the inlet velocity, v_{in}, and 2) the inlet equivalence ratio, ϕ. The enhanced thermal performance is quantified by the increased mean wall temperature and the increased wall temperature uniformity. We find that thermal performance increases with increasing v_{in}. The maximum level of NO is present at $v_{in} = 2$ m/s. Meanwhile, the mean wall temperature benefits from $\phi = 1$, and further increases in equivalence ratio can lessen the uniformity of the wall temperature. Furthermore, more fuel-rich ammonia combustion can lead to a lower NO emission and improve the thermal performance. To enhance ammonia combustion, further investigations are conducted by blending with different molar fractions of H_2 (X_{H_2}). It is found that mixing ammonia with more H_2 can stabilize micro-combustion, and increase the temperature in the combustion field. Additionally, it makes the emission worse. The maximum mean wall temperature occurs at $X_{H_2} = 0.25$, While the NO emission peaks at $X_{H_2} = 0.3$. Moreover, the OH mole fraction can affect the formation of NO, positively.

1. Introduction

The combustion of carbon-based fuels, which generates greenhouse gases (GHG) and causes subsequent effects of climate change, has become a challenge for researchers to overcome [1]. According to the Paris climate agreement [2], global warming should be limited to below two degrees Celsius, and the target is to decrease GHG to 50 % by 2030. To reach these targets, the combustion fuelled by carbon-free fuels has attracted broad attention for advancing the commercial application of carbon-free fuels, such as hydrogen, ammonia, and so on. Since hydrogen has a high energy density and its product of combustion fuelled by hydrogen is primarily water, it shows great promise to reduce the emissions of GHG. However, it is laborious to store and transport hydrogen due to its high volatility with a fast laminar burning rate and a low flash point [3]. in contrast, ammonia is much more stable and it products of reaction are limited to Nitrogen and water making it an attractive alternative to hydrogen [4]. Moreover, ammonia is in its

liquid phase at 273 K and at only 8 atm [5], which decreases the difficulty of storing and shipping compared to hydrogen [6]. Additionally, ammonia can be synthesized by the Haber-Bosch process commercially [7], which employs the direct reaction $N_2 + 3H_2 \rightarrow 2NH_3$ under the environment of high pressure(100–100 atm) and high temperature (673–823 K).

There remain challenges to the adoption of ammonia as a fuel, such as the low burning velocity [8], the ignition delay [9], and the production of producing a large amount of oxynitride [10]. Due to the stringent emission regulations aiming to reduce greenhouse gases, there is an increasing interest in improving the reactivity of burning ammonia. Research into the combustion of ammonia to power aircraft engines can be found as early as 1966 [11]; it was initially proposed to power aircraft engines, such as gas turbine engines, in the military domain. Early tests indicated that engines fuelled by ammonia have a lower power output (compared to hydrocarbon-fuelled engines) as a result of the lower reactivity of burning ammonia. Blending ammonia with hydrocarbon fuels has been proven effective in increasing the reactivity of burning

Nomenclature

A_i	Surface area of mesh element
$C_{\varepsilon 1}$	Constant
$C_{\varepsilon 2}$	Constant
C_μ	Model constant
e	Specific internal energy [kJ]
h	Natural convection heat coefficient (10 W/$m^2 \bullet K$)
h_l	Specific enthalpy of species l [J/kg]
J_l	Diffusive flux of species l
k	The turbulent kinetic energy
k_e	Thermal conductivity [W·m-1·K-1]
m_l	Molecular weight of the spice of l
m_{tot}	Total amount of molecular of all species
M	Molar mass in an absolute system
N	Total number of grids on the surface
$\overline{P}$	Time averaged pressure [Pa]
P_k	Production term
q	Heat loss[W]
R_l	Production rate of species of l
R	Universal gas constant [8.3145(J/(mol·K)]
S_h	Source term
T	Temperature [K]
$\overline{T}_w$	Mean wall temperature [K]
T_i	Wall temperature of mesh element [K]
ΔT_w	Deviation of wall temperature [K]
T_W	Outer-wall temperature [K]
T_E	Ambient temperature [300 K]
$\overline{\mathbf{u}}$	Time averaged velocity [m/s]
X_l	Mole fraction of species l
τ	Viscous stress
τ'	Reynolds stress
$\otimes$	Outer vector product

Greek letters

ε_e	Emissivity of the solid surface [0.85]
ε	Turbulent dissipation rate
μ	Dynamic viscosity [N·s/m2]
μ_t	Turbulent viscosity
ρ	Gas density [kg/ m3]
σ_k	Constant
σ_ε	Constant
σ_b	Stephan-Boltzmann constant [$5.67 \times 10^{-8} W/m^2 \bullet K^4$]
ϕ	Equivalent ratio of mole fraction

Abbreviation

MWT	Mean wall temperature [K]
SDWT	Standard deviation of wall temperature [K]
v_{in}	Inlet velocity [m/s]

ammonia. Co-firing hydrogen/ammonia in the heavy-duty engine was explored by Boretti et al. [12] who found that adding hydrogen improves the reaction rate of burning ammonia and that the energy conversion efficiency can be increased above 45 %. Furthermore, Boretti et al. [13] experimentally studied advanced turbocharging direct injection (TDI) engines by employing diesel and ammonia and showed that advanced TDI engines fuelled by diesel and ammonia possess a similar thermal performance compared to that powered by diesel in terms of efficiency and power densities. In addition, Mørch et al. [14] conducted a co-combustion of hydrogen/ammonia and found that at a hydrogen volume of 10 %, the spark ignition (SI) engine performs the best with respect to power output and efficiency. Ryu et al. [15] investigated a spark-ignition engine experimentally, proving that utilizing ammonia is feasible in such an engine while bending gasoline with ammonia can improve the burning velocity. Moreover, Kurata et al. [16] employed ammonia/air in a 50 kW gas turbine system. They showed the combustion efficiency can be up to 96 % at 80,000 rpm. Dai et al. [17] analysed the ignition delay of ammonia and ammonia/hydrogen numerically and experimentally in a rapid compression machine and showed that hydrogen plays an essential role in reducing the ignition delay of ammonia.

The production of NO$_X$ associated with the combustion of ammonia has also been studied extensively. Numerous studies have explored the formation of oxynitride from burning ammonia. The study of Honzawa et al. [18] considered the combustion of ammonia/methane/air and suggested that cold walls and radiation affect the emissions of NO$_X$ and CO, negatively. Pugh et al. [19] considered burning ammonia/hydrogen in a turbulent swirl combustor. Their results indicated that the NO$_X$ emission can be reduced with higher equivalence ratios and with higher burner pressures. Reiter et al. [20] studied the effect of blending ammonia with diesel in a four-cylinder engine. Their results showed that reduced NO_X emission can be achieved if ammonia accounted for less than 40 % of the premixed diesel fuel, and lower NO_X formation at lower combustion temperatures. Somarathne et al. [21] studied the emission characteristics of burning ammonia in a gas turbine and found that the increase in inlet pressure can lower the formation of NO_X. Okafor et al.

[22] expressed that the structure of inclined fuel injection, lean combustion of ammonia and increasing ambient pressure can reduce the emission of NO_X. In order to predict the formation of NO_X accurately, Konnov et al. [23] developed a detailed reaction mechanism of NO_X production relating to NCN for better predicting the reaction rate of $2CH + N2 = NCN + H$. Duynslaegher et al. [24] introduced a reduced reaction mechanism of ammonia validated by experimental results in a spark ignition engine and predicted the reaction pathway of nitrogen oxides. To better understand the reaction of burning ammonia numerically, especially at high pressure, Okafor et al. [25] developed a reduced mechanism of CH_4/NH_3/Air at different equivalence ratios and pressure. Further, they analysed the burning velocity of CH_4/NH_3/Air flames, NO concentration and CO concentration in a constant volume chamber. Xiao et al. [26] developed and validated a reduced mechanism of ammonia/hydrogen/Air combustion. Further, Meng et al. [27] developed a chemical reaction mechanism with 221 species and 1597 reactions to predict the emission of NO_X fuelled by NH_3/ dimethyl ether (DME) and found that lower DME content in the premixed dual fuel is beneficial in inhibiting the formation of NO_X. To achieve the target of reducing the computational time of simulating burning ammonia, Sun et al. [28] introduced a reaction mechanism comprising of only 19 species and 63 elementary reactions. Liukkonen et al.[29] utilized a sub-model-based artificial neural network approach to predict the emissions of NO$_X$ in a circulating fluidized bed boiler, and the methods had been proven applicable to explore the environmental emissions. Krzywanski et al. [30] introduced a method of Artificial Neural Network to analyse the formation of NO$_x$ in circulating fluidized bed combustors fuelled coal, aiming to provide a approach to simulating the emission of NO_X quickly and simply, and found that the results obtained from the method are credible compared with experimental data. Furthermore, Krzywanski et al. [31,32] developed an approach of fuzzy logic to explore the emissions of CO$_2$, CO, NO$_x$ and SO$_x$ to simplify the complex process of oxyfuel combustion and chemical looping combustion.

Burning ammonia in micro-power systems has attracted much attention. Iki et al. [33] successfully tested co-firing kerosene and ammonia in a micro-scale gas turbine and achieved a power output of up
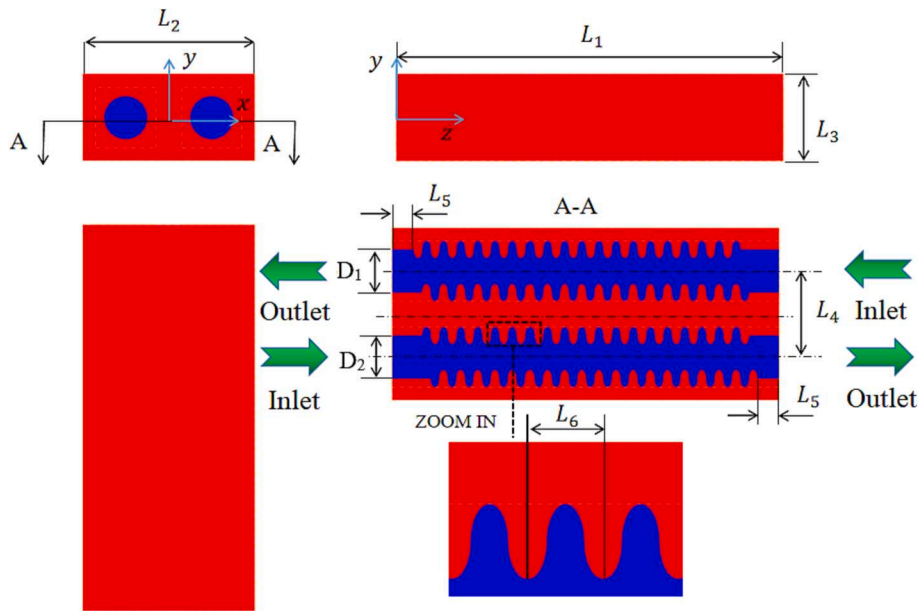
Fig. 1. Structure of double-channel micro-combustor with oval shaped threads.

to 40 W. Nakamura et al. [34] experimentally explored the ignition delay and burning velocity of premixed ammonia/air in a microflow reactor and further develoed the chemical kinetic model of the *N2Hx*chemistry. Okafor et al. [35] studied the co-firing methane/ammonia and burning ammonia to reduce the emissions of oxynitride in a micro gas turbine swirl combustor experimentally and numerically. The results showed that the formation of NO_X can be restrained at the equivalence ratios between 1.3 and 1.35, and that adding methane in the ammonia/air mixture can limit the formation of NO_X. For promoting the micro-scale power system, Cai et al. [36] developed a micro-combustor fuelled by ammonia. By changing the equivalence ratios of ammonia and oxygen, inlet pressure, and inlet temperature, it was found that the best thermal performance can be achieved at equivalence ratio = 0.9 with regard to increasing the wall temperature of the micro-combustor, the formation NO_X can be mitigated by optimizing the equivalence ratio, inlet pressure, and inlet temperature. The micro-scale power system (MSPS) fuelled by hydrogen and hydrocarbon fuels has also been studied recently. The combustion stability of hydrogen in MSPS is better than that of carbon-based fuels [37,38]. Adding catalysts in a micro-combustor has been shown to be able to enhance the stability of the micro-combustion distinctively [39–41]. Moreover, adding ribs [42], fins [43], a porous medium [44], and preheating channels [45] have also been shown to stabilize the combustion in the micro-combustors. Further, Zhang et al. achieved higher combustion efficiencies by adding a novel helical-fin in a micro-step Helix combustor [46].

To the best of our knowledge, to date only Cai et al. [36] explored the thermal performance and emission of NO_X in MSPS. The current work seeks to further investigate the parameters in the combustion of ammonia in a micro combustor that can lead to improved efficiency and reduced NO_X formation.

Previous studies [43,44] have shown that the double-channel combustor can increase the wall temperature [47]. Additionally, it has been shown that the mean wall temperature and wall temperature uniformity are higher for an oval shaped internal wall than for an rectangular and triangular-shaped internal wall [48]. Therefore, in this work, the double-channel micro combustor with the oval-shaped internal wall is chosen for exploring the thermal performance and the characteristics of NO emission in the combustion of hydrogen/ammonia/oxygen. The 3D structure of the micro-combustor with oval-shaped internal walls is presented and the governing equations of the model of this study are described and then validated in Section 2. The influences

of inlet velocity and equivalence ratio are presented in Section 3. Section 4 presents an investigation on the blending of ammonia with hydrogen.

2. Numerical method and thermal performance definition

2.1. Model description

In this work, a double-channel micro combustor with oval-shaped internal threads is chosen. A schematic diagram with relevant dimensions is illustrated in Fig. 1. The width (L_1), length (L_2) and height (L_3) of that combustor are 8 mm, 18 mm, and 4 mm, respectively. The combustor has two inner channels, and the distance between the centerlines of the two channels (L_4) is 4 mm. The inlet and outlet diameters (D_1) and (D_2) are both set at 2 mm. The outline of the oval-shaped thread is shown in the close-up (bottom right) for which a and b represent the major axis and minor axis of the oval thread (their lengths are 0.4 mm and 0.2 mm, respectively). Meanwhile, the space (L_6) between the oval-shaped threads is 0.4 mm. For better stabilizing the combustion on the developed micro-combustor, the length L_5 at the inlet/outlet is 1 mm. The total length of the oval-shaped threads is set as 16 mm.

2.2. Governing equations and thermal performance definition

The numerical simulations are conducted by assuming a steady incompressible three-dimensional flow with the standard $k-\varepsilon$ turbulence model.

The conservation equations of continuity and momentum are shown in tensor notation as follows:

$$\rho \nabla \bullet \overline{\mathbf{u}} = 0 \tag{1}$$

$$\rho \overline{\mathbf{u}} \bullet \nabla \overline{\mathbf{u}} = -\nabla \overline{P} + \nabla \bullet (\tau - \tau^{'}) \tag{2a}$$

$\overline{\rho \mathbf{u}' \otimes \mathbf{u}'}$ can be expressed as:

$$\overline{\rho \mathbf{u}' \otimes \mathbf{u}'} = \frac{2}{3}\rho k - \mu_t\left(\nabla \overline{\mathbf{u}} + (\nabla \overline{\mathbf{u}})^T\right) \tag{2b}$$

μ_t is shown as:

$$\mu_t = \rho C_\mu \frac{k^2}{\varepsilon} \tag{2c}$$

The transport equation for *k* is:

Table 1

Inlet boundary conditions corresponding to different testing cases.

No.	$v_{in}(m/s)$	X_{NH_3}	X_{H_2}	X_{O_2}	Φ
1	1	0.4	0.2	0.4	1
	2	0.4	0.2	0.4	1
	3	0.4	0.2	0.4	1
	4	0.4	0.2	0.4	1
	6.5	0.4	0.2	0.4	1
2	2	0.39226	0.15	0.45774	0.8
	2	0.41864	0.15	0.43136	0.9
	2	0.44285	0.15	0.4071421	1
	2	0.46527	0.15	0.38473	1.1
	2	0.48615	0.15	0.36385	1.2
3	2	0.57143	0	0.42857	1
	2	0.52857	0.05	0.42143	1
	2	0.48571	0.1	0.41429	1
	2	0.44285	0.15	0.40714	1
	2	0.4	0.2	0.4	1
	2	0.35714	0.25	0.39286	1
	2	0.31429	0.3	0.38571	1

$$\rho\overline{\mathbf{u}} \bullet \nabla k = \nabla \bullet \left(\left(\mu + \frac{\mu_t}{\sigma_k} \right) \nabla k \right) + P_k - \rho\varepsilon \tag{2d}$$

where P_k can be expressed as:

$$P_k = \mu_t \left(\overline{\mathbf{u}} : \left(\nabla\overline{\mathbf{u}} + (\nabla\overline{\mathbf{u}})^T \right) - \frac{2}{3}\rho k \nabla\overline{\mathbf{u}} \right) \tag{2e}$$

The transport equation for ε is:

$$\rho\overline{\mathbf{u}} \bullet \nabla\varepsilon = \nabla \bullet \left(\left(\mu + \frac{\mu_t}{\sigma_\varepsilon} \right) \nabla\varepsilon \right) + C_{\varepsilon 1}\frac{\varepsilon}{k}P_k - C_{\varepsilon 2}\rho\frac{\varepsilon^2}{k} \tag{2f}$$

The conservation of energy is:

$$\nabla \bullet (\rho\overline{\mathbf{u}}e) = -\nabla \bullet P\overline{\mathbf{u}} + \nabla \bullet \left(k_e\nabla T - \sum h_l\mathbf{J}_l + \tau \bullet \overline{\mathbf{u}} \right) + S_h \tag{3}$$

The conservation of species l is represented by:

$$\nabla \bullet (\rho\overline{\mathbf{u}}X_l) = -\nabla\mathbf{J}_l + R_l \tag{4}$$

The equation of thermodynamic state is written as:

$$P = \rho\frac{R}{M}T \tag{5}$$

The indexes of the mean wall temperature (MWT) and standard deviation of wall temperature (SDWT) are important measures to determine the efficiency of the micro-combustor. Further, increasing MWT and reducing the SDWT help improve the efficiency of micro-combustor. Thus, MWT and SDWT are introduced to explore the thermal characteristics of the micro-combustor with oval-shaped threads fueled by premixed ammonia/hydrogen/oxygen [48].

$$\overline{T}_w = \frac{\sum A_i T_i}{\sum A_i} \tag{6a}$$

$$\Delta T_w = \sqrt{\frac{\sum_{i=1}^{N}(T_i - \overline{T}_w)^2}{N}} \tag{6b}$$

The heat loss affected by the ambient environment is expressed as:

$$q = h(T_W - T_E) + \varepsilon_e\sigma_b(T_W^4 - T_E^4) \tag{7}$$

In this work blending hydrogen is to improve the combustion stability of burning ammonia. The moile fraction, X_l, is defined as:
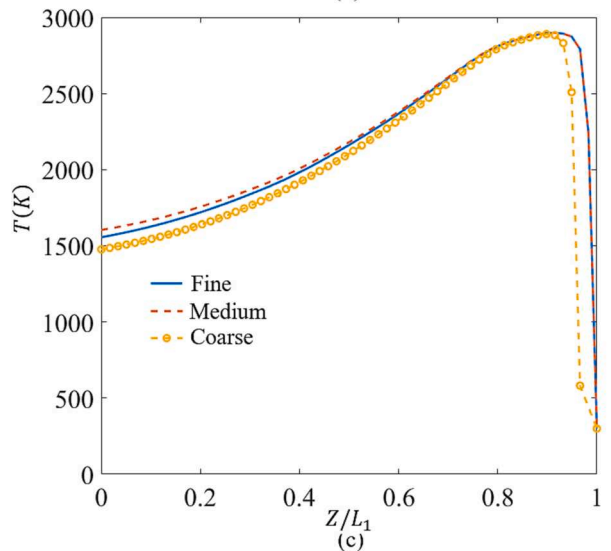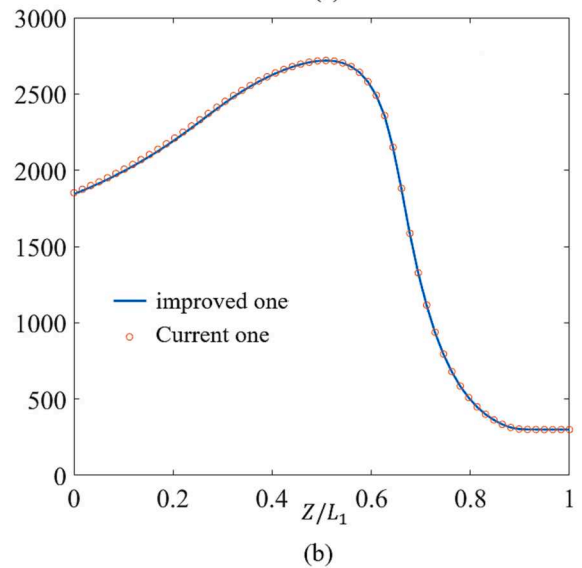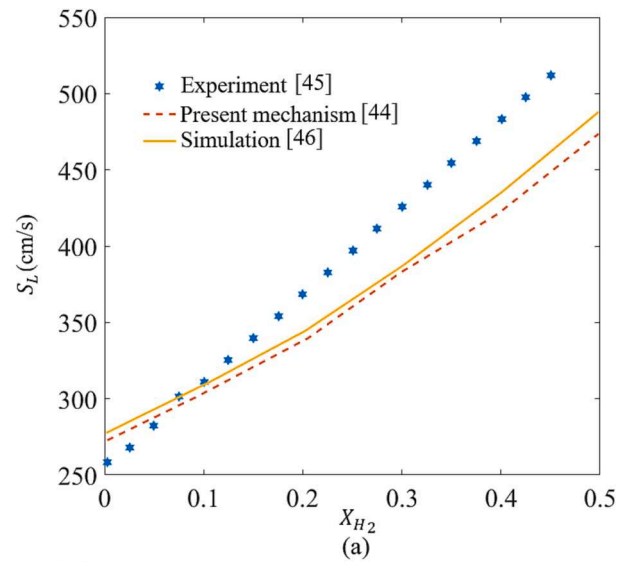
$$X_l = \frac{m_l}{m_{tot}} \tag{8}$$

Fig. 2. (a) the laminar flame speed of $NH_3/H_2/air$ premixed flame at $\Phi = 1.0$ as a function of X_{H_2}. (b) comparison of the central line temperature for combustion channel between the different residuals. (c) comparison of the central line temperature for combustion channel between the different meshes. Here the inlet corresponds to the dimensionless axial position $Z/L_1 = 1$.

Table 2
The boundary conditions of the chosen case:

$v_{in}(m/s)$	X_{NH_3}	X_{H_2}	X_{O_2}	Φ
2	0.57143	0	0.42857	1

The effect of the inlet velocity (v_{in}), the equivalent ratio (Φ) of the mole fraction between ammonia/hydrogen and oxygen, and the mole fraction (X_{H_2}) between hydrogen and other species are conducted. The inlet boundary conditions are divided into three groups numbered 1, 2, and 3. more details are listed in Table.1.

To examine the NO emission and thermal performances on the double-channel micro combustor with oval-shaped threads, a commercially available CFD platform, ANSYS-Fluent version R2021, is used to evaluate Eqs. (1)-(8) numerically. According to the previous studies [49,50], the standard k-ε model and the eddy dissipation concept (EDC) model has been proven applicable for the micro-combustion fuelled by hydrogen. Thus, in this work, the standard k-ε model and the eddy dissipation concept (EDC) model are used for the simulations of the ammonia/hydrogen micro-combustion. For the numerical simulation, the -ideal-gas law, the mixing-law model, and pressure-based COUPLE algorithm are employed while a 2nd order upwind method is utilized to solve all the aforementioned equations. The absolute criteria of convergence of continuity, velocity, and species are set at 10^{-3} while the absolute criterion of energy is set at 10^{-6}. A velocity inlet and pressure outlet are used for the momentum boundary conditions. The hydraulic diameter and the turbulent intensity of the inlet and outlet are set as 2 mm, and 5 %, respectively. The material property of the developed combustor selected as steel, with a heat transfer coefficient and an external emissivity of10 W/m^2 K and 0.85, respectively. In order to avoid reverse flow, the mole fraction of O_2 is set as 0.21 at the outlet. The ammonia chemical mechanism with 19 species and a 63 step chemical reaction that was introduced and validated by Sun et al. [28] is used in the current study. A comparison of the chemical mechanism [28] with the experimental [51] and the previous simulation data [52] is

shown in Fig. 2 (a). Results indicate that the chemical mechanism not only can reduce computational time but also promise the accuracy of the laminar flame speed, S_L. Sun et al. [28] utilized the ANSYS Fluent 19.0 and Chemkin to calculate the laminar burning speed of ammonia, which blends with hydrogen. The initial condition of calculating the laminar burning speed is at atmospheric pressure. The inlet temperature is set to 300 K. Meanwhile the inlet and outlet of the combustor boundary conditions are set to velocity inlet and pressure outlet with constant relative pressure 0 Pa. It should be noted that the laminar burning speed of ammonia/hydrogen shows a similar trend as the experimental data. Furthermore, the maximum blending ratio of hydrogen in the premixed ammonia/oxygen/hydrogen mixture considered in this work is 35 %, whose laminar burning speed difference between that of experimental data is less 10 %. Thus, the chemical mechanism is assumed to be reasonably applicable for the present investigations using Fluent 2021.

It is beneficial of reducing residuals to simulate micro-combustion fuelled by ammonia. The chemical mechanism of burning ammonia contains 19 species, and 63 reactions, which consumes a large amount of computational time. Thus, it is necessary to figure out the influence of the absolute criteria of convergence, continuity, velocity, species and energy. One of the current cases is chosen to compare the influence of different residuals, and the absolute criteria of convergence, continuity, velocity, and species of the improved one are set as 10^{-5}, while the absolute criterion of energy is 10^{-6}. The boundary conditions of the chosen cases are listed in Table 2. As shown in Fig. 2(b), the temperatures along the combustion channel central line of the two cases are compared. The biggest temperature difference between the two cases is less than 0.5 %. Thus, the absolute criteria of convergence, continuity, velocity, and species setting as 10^{-3} are enough for the present investigations.

2.3. Grid independence

Fig. 2 (c) shows the comparison of the centerline temperature profiles of the two-channel combustor obtained from three different sizes of mesh: coarse (8,683,734 nodes), medium (15,268,307 nodes), and fine
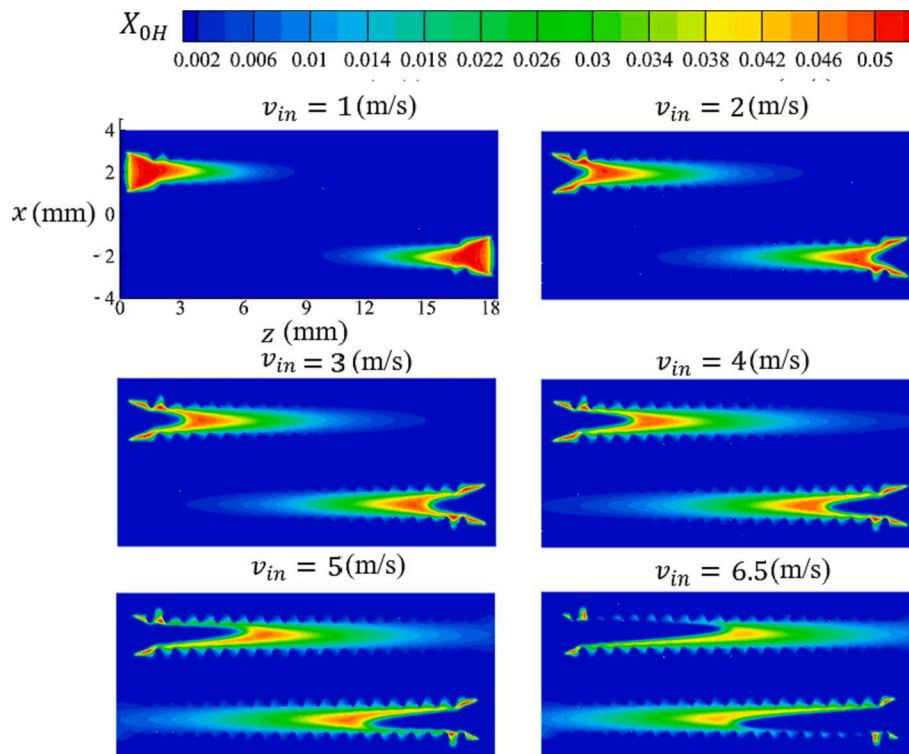

Fig. 3. Variation of the **OH** mole fraction in the counter-flow micro-combustors with the oval-shaped internal threads under the different inlet velocity.
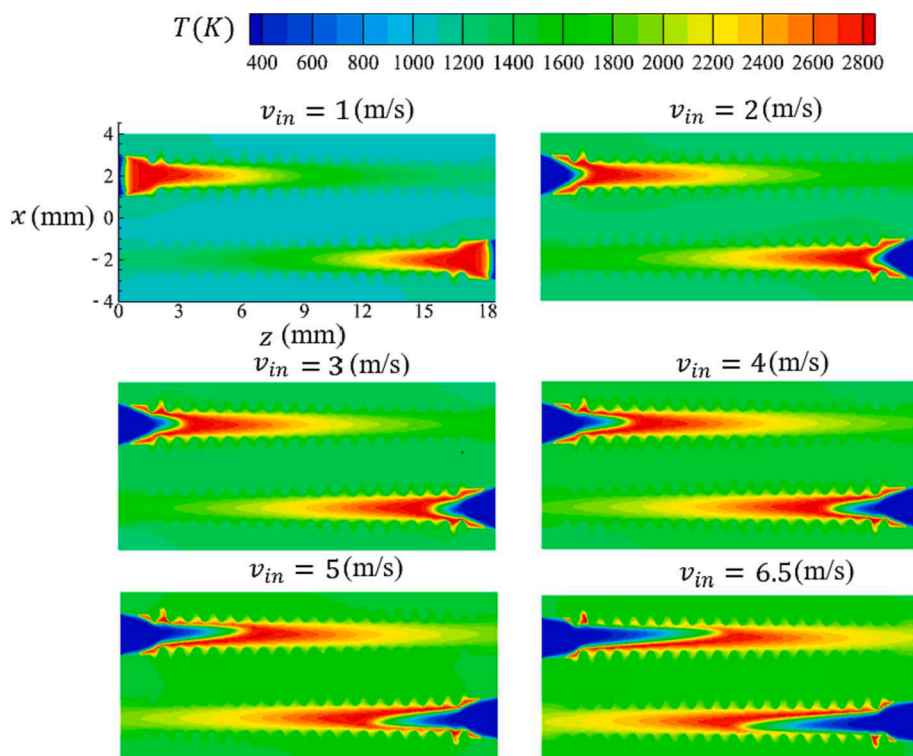
Fig. 4. Variation of the flame temperature contours of the counter-flow micro-combustors with oval-shaped internal threads under the different inlet velocity.
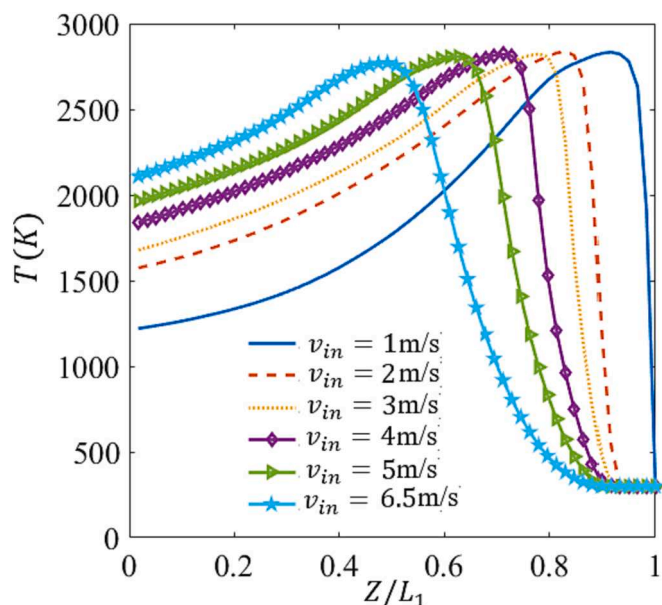

Fig. 5. Numerical predicted flame temperature along the centerline of different inlet velocities. Here the inlet corresponds to dimensionless axial position $Z/L_1 = 1$.

(20,321,021 nodes). In the cases shown in Fig. 2 (b), the inlet velocity is 2 m/s, and the equivalence ration (Φ) between NH_3 and O_2 is set as 1. Further, the H_2 mole fraction at the inlet is 0.25. Although the medium and fine meshes have a similar tendency, the coarse mesh exhibits a different trend. In addition, the temperature differential between medium and fine mesh is largest at the combustion channel outlet, around 42 K, or less 3 % of the temperature at the outlet of medium mesh. The author is not aware of any published experimental data focusing on micro-combustion powered by ammonia. In the current cases, the Fluent set is the same with Shen et al. [53], which have demonstrated that the simulation set can guarantee the correctness fuelled by premixed H_2/Air compared to the experimental data in Ref. [53]. Thus, the medium mesh is chosen to shorten computing time because the outcomes of the current medium mesh simulation are satisfactory.

3. Results and discussion

3.1. The effect of the inlet velocity v_{in}

This section examines the impact of the inlet velocity, v_{in} to analyze thermal performance and NO emission. At the inlet, the v_{in} is set as 1, 2, 3, 4, 5, and 6.5 m/s, respectively. The corresponding ratio (Φ) is set to 1 to examine the impact of v_{in}. The H_2 mole fraction (X_{H_2}) at the inlet is set as 0.2 for improving the combustion stability of burning premixed NH_3/O_2. According to Stelzner et al. [54], the OH mole fraction can be employed to determine the position of flame. As the input velocity increases, Fig. 3 demonstrates that the position of the premixed flame tends to shift downstream. Furthermore, the OH mole fraction peak shrinks, as v_{in} is rising. The temperature on the micro-combustor similarly experiences the phenomenon, where the temperature peak migrates downstream as shown in Fig. 4.

The temperature distributions along the combustion channel centerline depicted in Fig. 5 for all cases show a sudden increase near the inlet. However, the temperature peaks corresponding to the inlet flow velocity being set to 1 m/s, 2 m/s, 3 m/s, 4 m/s, 5 m/s, and 6.5 m/s are observed to occur at $Z/L_1 = 0.91, 0, 0.83, 0, 0.78, 0, 71, 0, 61,$ and $0, 49$, respectively and at these locations, the temperature values are 2771 K, 2808 K, 2822 K, 2823 K, 2839 K, and 2834 K. These results indicate that increasing v_{in} shifts the flame position downstream and increases the peak temperature. However, care should be taken when interpreting these results because the maximum temperatures vary by less than 2.5 % over the range of inlet velocities considered. The highest temperature is increased by the growth of v_{in} prior $v_{in} = 5$ m/s. However, the highest temperature associated with $v_{in} = 5$ m/s is still 5 K higher than that associated with $v_{in} = 6$ m/s. These results indicate that increasing v_{in} can

Table 3
MWT and SDWT of different inlet velocities.

v_{in}(m/s)	1	2	3	4	5	6.5
MWT(K)	1076	1272	1343	1429	1484	1548
SDWT(K)	22	23	28	29	29	32

intensify the phenomenon of blow-off.

Table 3 depicts the variations of MWT and SDWT at different v_{in}. These results indicate that increasing v_{in} results in an increased MWT. While the results show that the uniformity of the wall temperature decreases with increasing inlet velocity, it is important to note that the SDWT varies by only 13 K over the range of inlet velocities considered.

Fig. 6 illustrates the unburnt NH_3 contours at different inlet velocities. It is worth noting that the area of unburnt NH_3 increases with increasing v_{in}. The profile shape of the NH_3 mole fraction is triangular, which means the highest temperature concentrates in the center of the micro-combustion channel. Furthermore, the profile area of unburnt NH_3 decreases with increasing inlet velocity, which means micro-combustion fuelled by ammonia is very sensitive to the inlet velocity.

Following the previous work by Glarborg et.al [55], NO_2 the concentration of NO may be used as an indicator of the emissions of NO_x. Fig. 7 shows NO mole fraction along the centerline of cases with different inlet velocities. In all cases, the X_{NO} experiences a rise near the inlet to an inflection followed by a slight drop that gradually plateaus towards the outlet. The gradients of X_{NO} near the inlet decrease with increasing inlet velocity so that the inflection point is shifted downstream with increasing inlet velocity. When $v_{in} = 6.5$, it is clear that the X_{NO} at the infection point is higher than that at the outlet, which indicates that the unburnt NH_3 mole fraction is increasing as increasing v_{in}.

Table 4 summarizes the NO mole fraction at the outlet under different inlet velocities. The emission of NO reaches its peak while $v_{in} = 2$ m/s. For v_{in} above 2 m/s, the NO tends to decrease, which is affiliated with strengthening the blow-off effect associated at higher v_{in}. Furthermore, the unburnt NH_3 mole fraction at the outlet is larger,
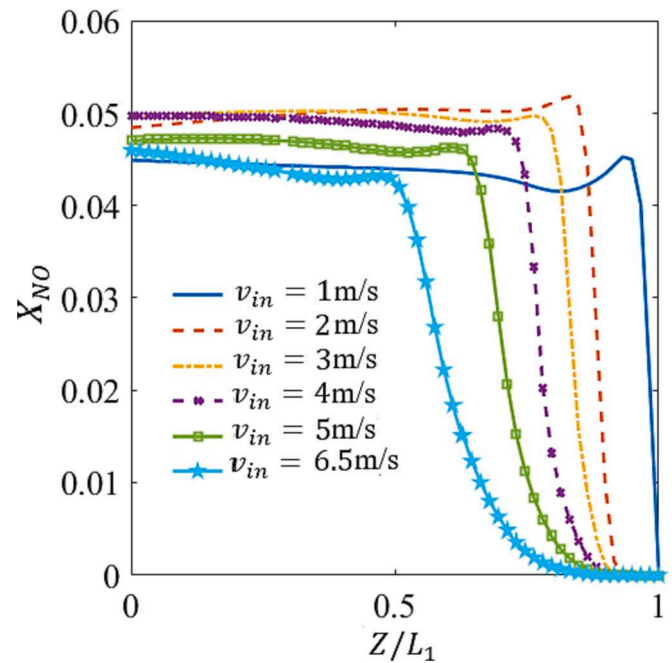

Fig. 7. Numerical predicted *NO* mole fraction along the centerline of different inlet velocities. Here the inlet corresponds to dimensionless axial position $Z/L_1 = 1$.

Table 4
NO mole fraction at outlet under different velocities.

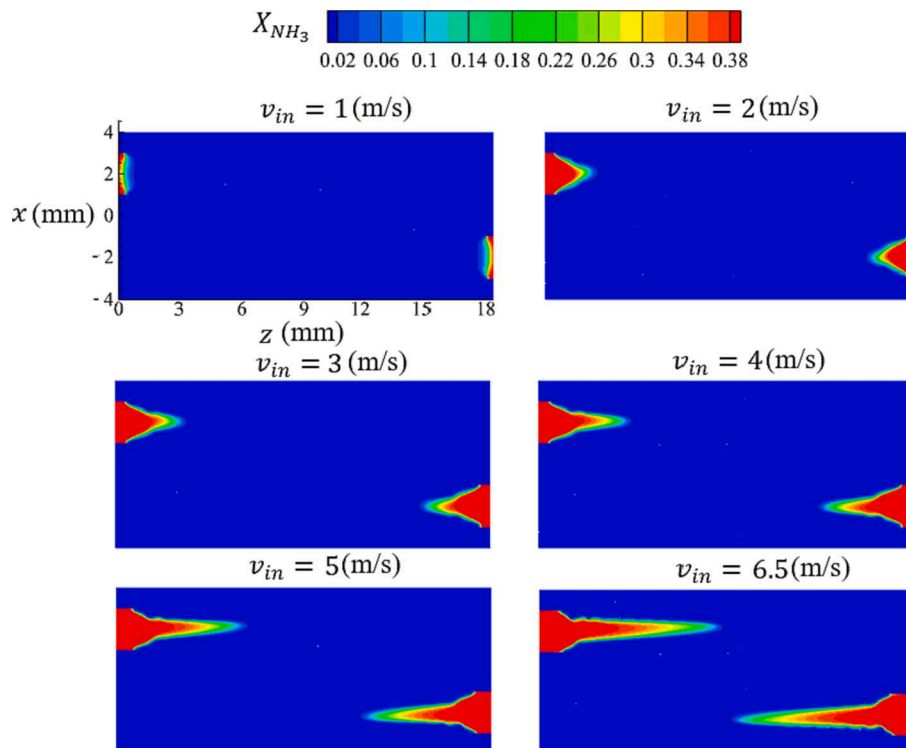| v_{in}(m/s)	1	2	3	4	5	6.5
NO	0.0453	0.05161	0.04978	0.04837	0.04635	0.0432

Fig. 6. Variation of the unburnt NH_3 mole fraction in the counter-flow micro-combustors with oval-shaped internal threads under the different inlet velocity.
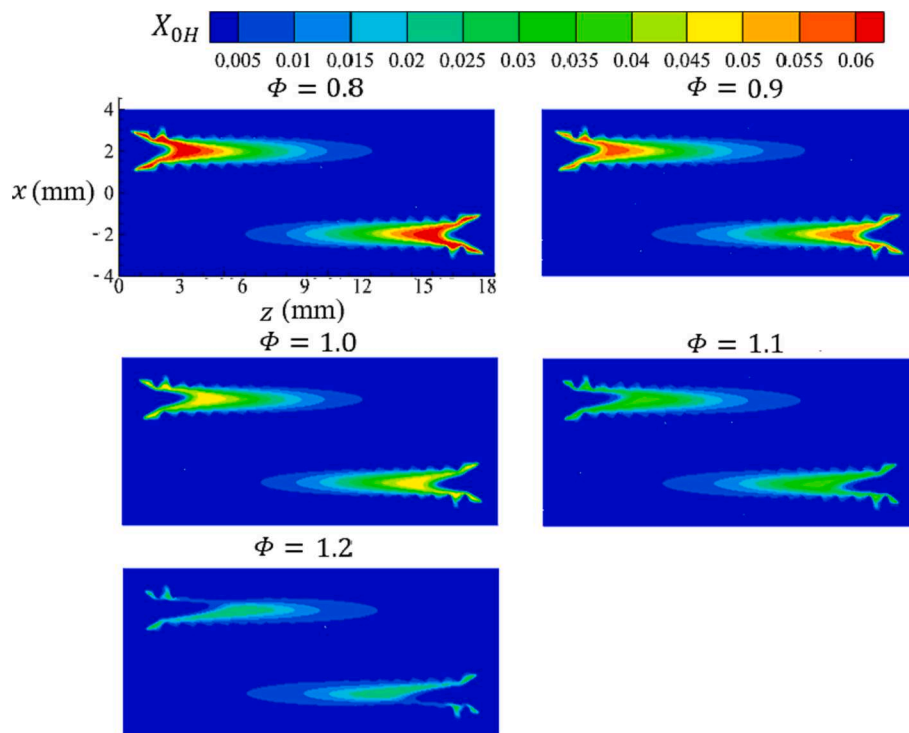
Fig. 8. Variation of the *OH* mole fraction in the counter-flow micro-combustors with the oval-shaped internal threads under inlet equivalent ratio.
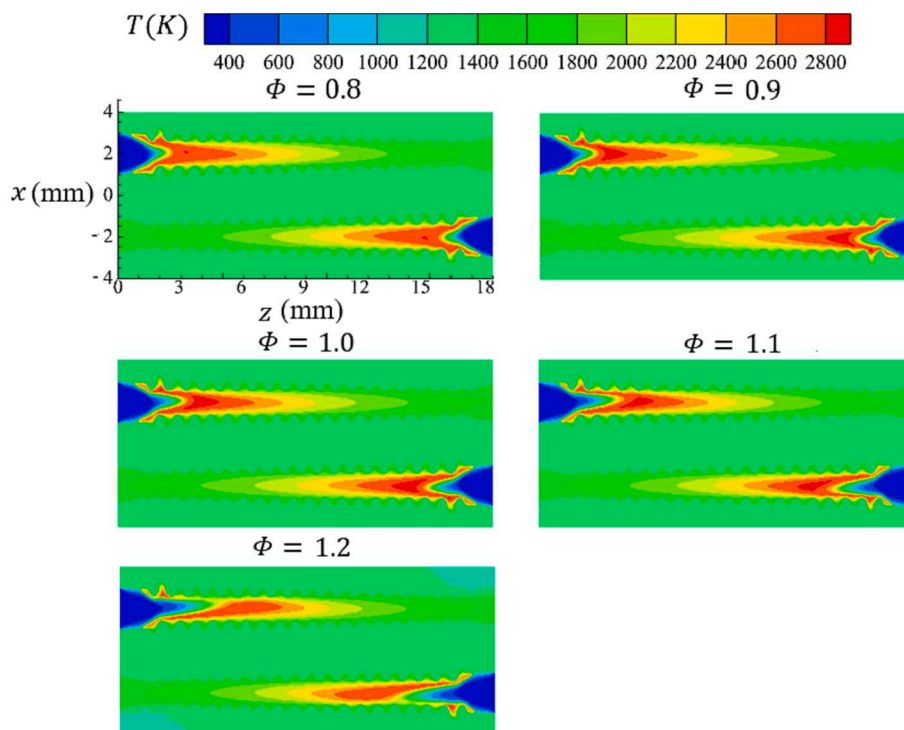

Fig. 9. Variation of the flame temperature contours of the counter-flow micro-combustors with oval-shaped internal threads under inlet equivalence ratio Φ.

which leads to a decrease in NO formation at the outlet. It should be noted that the NO mole fraction at the outlet of $v_{in} = 1$ m/s is lower than that of $v_{in} = 2$ m/s. The main chemical reaction area of $v_{in} = 1$ m/s occurs at the position between the oval thread and inlet and can react more completely than that of $v_{in} = 2$ m/s. Furthermore, the emission of NO at the combustor outlet can be reduced compared to that of $v_{in} = 2$ m/s.

A closer observation on Fig. 2 can help explain the changes of the NO emission with increased inlet velocity. In comparison with OH mole fraction in the micro-combustor of $v_{in} = 1$ m/s, the highest OH mole fraction of $v_{in} = 1$ m/s is almost the same with that of $v_{in} = 2$ m/s. However, the OH mole fraction area of $v_{in} = 2$ m/s is enlarged than that of $v_{in} = 1$ m/s, evidently. This contributes to the increase of NO emission
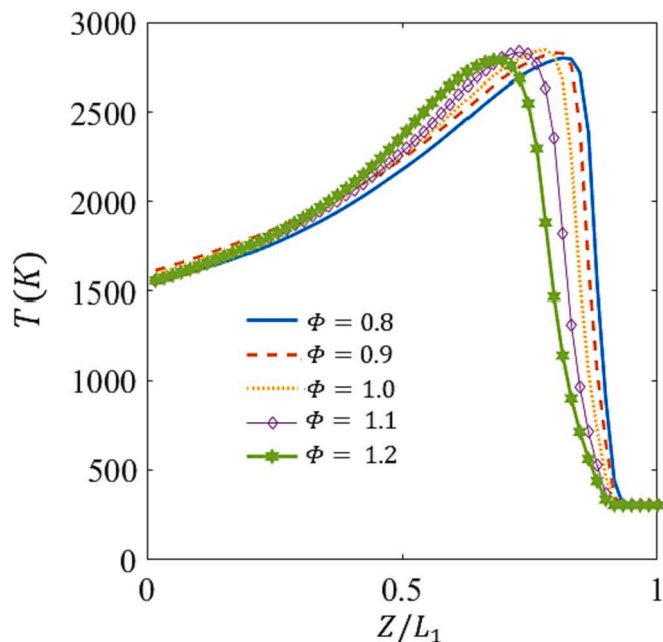
Fig. 10. Numerical predicted flame temperature along the centerline of different equivalent ratios under inlet equivalent ratio. Here the inlet corresponds to dimensionless axial position $Z/L_1 = 1$.

Table 5
MWT and SDWT of different inlet velocities.

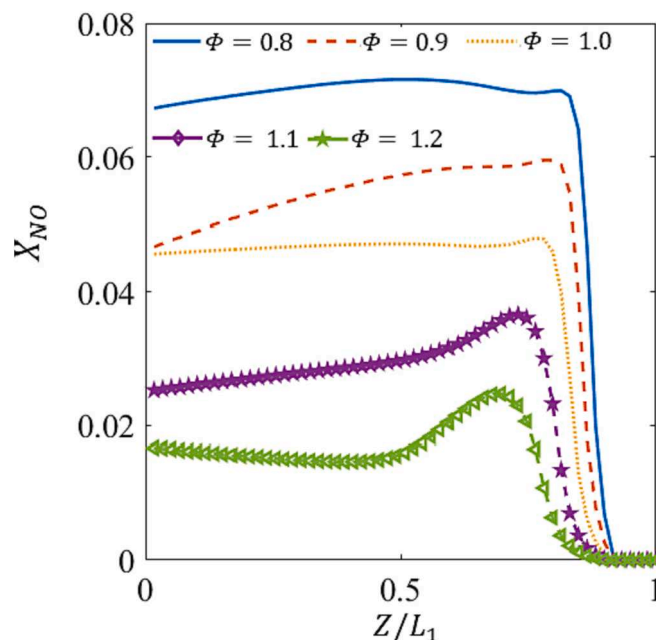| Φ	0.8	0.9	1	1.1	1.2
MWT(K)	1259	1276	1319	1243	1227
SDWT(K)	22.61	22.24	21.4	20.72	19.43

Fig. 12. Numerical predicted *NO* mole fraction along the centerline of different inlet velocities under inlet equivalent ratio. Here the inlet corresponds to dimensionless axial position $Z/L_1 = 1$.

Table 6
NO mole fraction at outlet under different equivalence ratios.

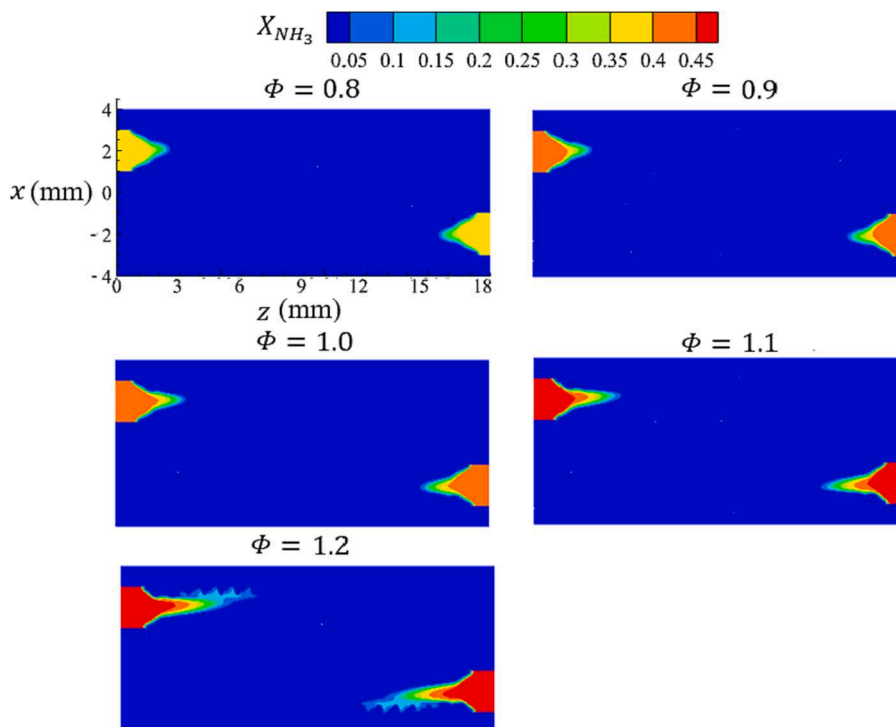| Φ	0.8	0.9	1	1.1	1.2
NO	0.06526	0.04309	0.04512	0.02389	0.01745

Fig. 11. Variation of the unburnt NH_3 mole fraction in the counter-flow micro-combustors with oval-shaped internal threads under inlet equivalent ratio.
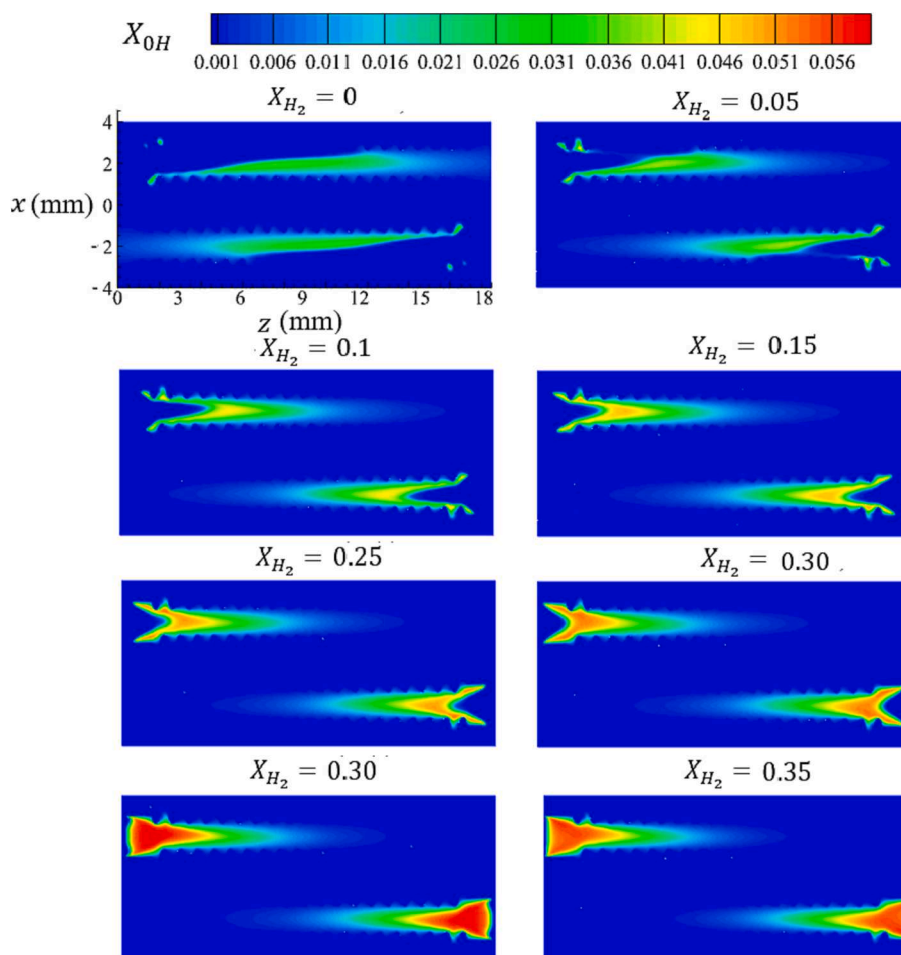
Fig. 13. Variation of the OH mole fraction in the counter-flow micro-combustors with the oval-shaped internal threads.

corresponding to the case of v_{in} = 2 m/s. It is clear that the OH mole fraction peak tends to decrease with increased v_{in}. However, it reduces the emission of NO.

3.2. The effect of equivalence ratio Φ

This section investigates on how the equivalence ratio affects thermal performance and NO production. The range for the equivalence ratio (ER) is set between 0.8 and 1.2. More details of the inlet boundary are listed in Table 1.

Fig. 8 presents the variation of the OH mole fraction in the counter-flow micro-combustors with the oval-shaped internal threads under different equivalent ratios (Φ). As the value of Φ grows, the flame's position barely alters. However, there is a significant reduction in the peak of the OH mole percentage due to the growth of Φ. Our results show that increasing Φ can restrain the formation of NO and reduce the emission of NO, which relates to reduced highest temperature. Thus, burning ammonia under fuel-rich conditions is more effective in mitigating *NO* emission.

Fig. 9 illustrates the variation of the flame temperature contours under different ER Φ. The position of the highest temperature nearly remains unchanged at Φ ≤ 1. However, when Φ > 1, the position of the peak temperature shifts downstream. It can be explained that lean-fuel combustion can slow down the burning velocity. Additionally, the lower burning velocity causes combustion to become unstable, particularly evident at Φ = 1.1 and 1.2. The present results indicate that the decreased highest temperature as increasing Φ reduces the stability of micro-combustion fuelled by ammonia.

To numerically investigate how the equivalent ratio affects thermal performance, Fig. 10 represents the flame temperature along the centerline of different equivalent ratios. The position of the highest temperature of Φ = 0.8, 0.9, 1.0, 1.1, and 1.2 is 0.8305, 0.8136, 0.7797, 0.7288 and 0.678, respectively. it is evident that the peak position is shifted downstream with increasing Φ. Moreover, the highest temperature of Φ = 0.8, 0.9, 1.0, 1.1, and 1.2 is 2794 K, 2826 K, 2845 K, 2833 K, and 2788, respectively. The peak temperature gets slightly higher when Φ approaches 1.0 (though in this range, the maximum temperature varies by less than 2%) . Combining with Fig. 8. it can be concluded that the position of flame is affected by varying Φ. Still, the chemical reaction of burning ammonia is strengthened by decreasing Φ, reflecting the decrease in maximum flame temperature with increasing Φ.

Table 5 summarizes the MWT and SDWT corresponding to different equivalence ratios ϕ. From Φ = 0.8 to Φ = 1.0, the MWT tends to increase and reach its highest value, at Φ = 1.0. with further increases (Φ >=1.0), the MWT starts to decrease. Besides, the SDWT tends to decline, as Φ is increased. However, the maximum SDWT is only 3.81 K higher than that of the minimum SDWT, so the changes in SDWT caused by rising Φ can be considered to be negligible. It can be explained by the fact that rich-fuel combustion can strengthen the chemical reaction of burning ammonia, contributing to the increased MWT as decreasing Φ. Moreover, it is shown that more lean-fuel combustion can force the highest temperature to move downstream, improving the uneven wall temperature distribution.

Fig. 11 depicts the variation of the unburnt NH_3 mole fraction in the counter-flow micro-combustors with oval-shaped internal threads. As Φ is increased, the highest NH_3 mole fraction tends to drop. This is due to
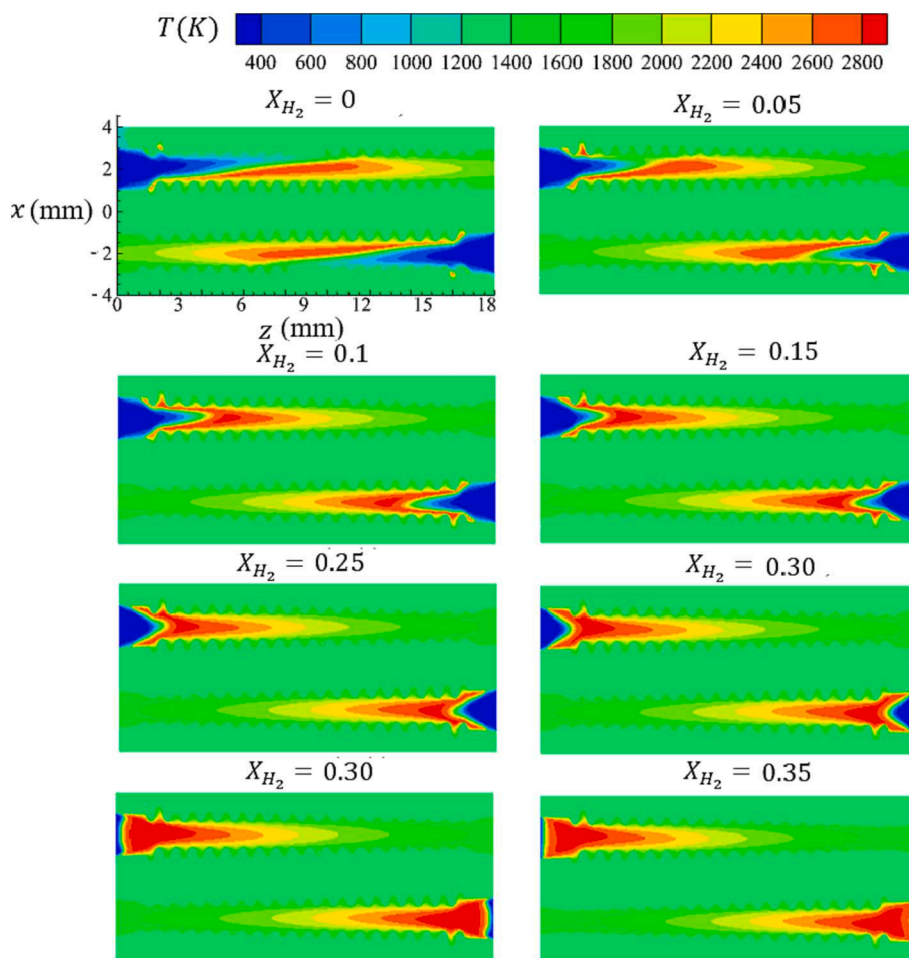
Fig. 14. Variation of the flame temperature contours of the counter-flow micro-combustors with oval-shaped internal threads.
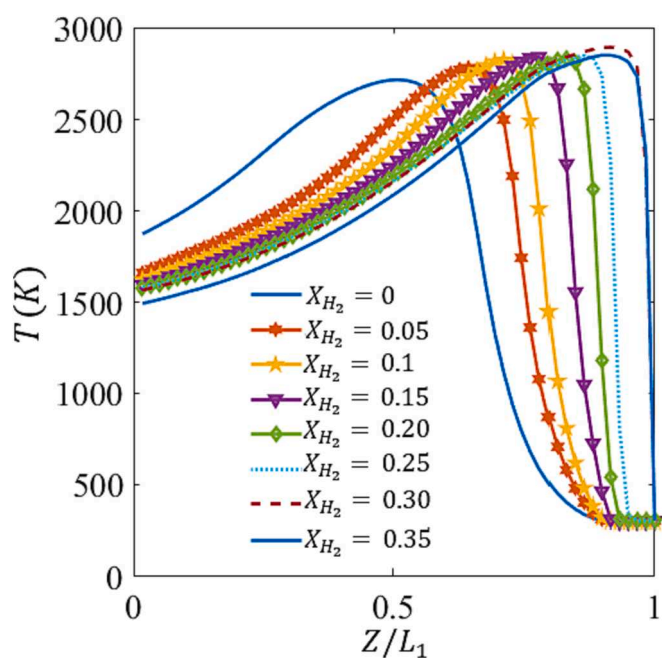

Fig. 15. Numerical predicted flame temperature along the centerline of different H_2 mole fraction at the inlet. Here, the inlet corresponds to dimensionless axial position $Z/L_1 = 1$.

Table 7
MWT and SDWT of different H_2 mole fraction at the inlet.

X_{H_2}	0	0.05	0.1	0.15	0.2	0.25	0.3	0.35
MWT(K)	1246	1263	1254	1265	1272	1281	1275	1250
SDWT(K)	20	21	21	21	23	25	28	30

the mole fraction differences of NH_3 at the outlet of $\Phi = 0.8$–1.2. When $\Phi > 1$, the highest NH_3 mole fraction moves downstream, as Φ is growing. This reveals that more lean-fuel combustion can lead to a decrease of burning velocity.

Fig. 12 illustrates the NO mole fraction along the centerline of different equivalent ratios. The inflection point is at 0.8136, 0.7966, 0.7797, 0.7288, and 0.6949, corresponding to $\Phi = 0.8$, 0.9, 1.0, 1.1, and 1.2, respectively. When the equivalence ratio is increased for $\Phi \leq 1$, the inflection point shifts downstream gradually. The downstream shift increases dramatically after $\Phi = 1$, which is also caused by lean-fuel combustion leading to the chemical reaction delay. The mole fractions at the inflection point are 0.02472, 0.03656, 0.04786, 0.05978, and 0.06992 corresponding to $\Phi = 0.8$, 0.9, 1.0, 1.1, and 1.2, respectively.

Table 6 shows the NO mole fraction at the outlet under different equivalence ratios. Our results indicate that increasing Φ can restrain the formation of NO and reduce the emission of NO, which relates to reduced maximum temperature. Thus, the burning of ammonia under fuel-lean conditions is more effective in mitigating NO emission. As revealed in Fig. 8, the combustion product of NO is affected by the OH mole fraction positively. The reduced OH mole fraction peak is caused
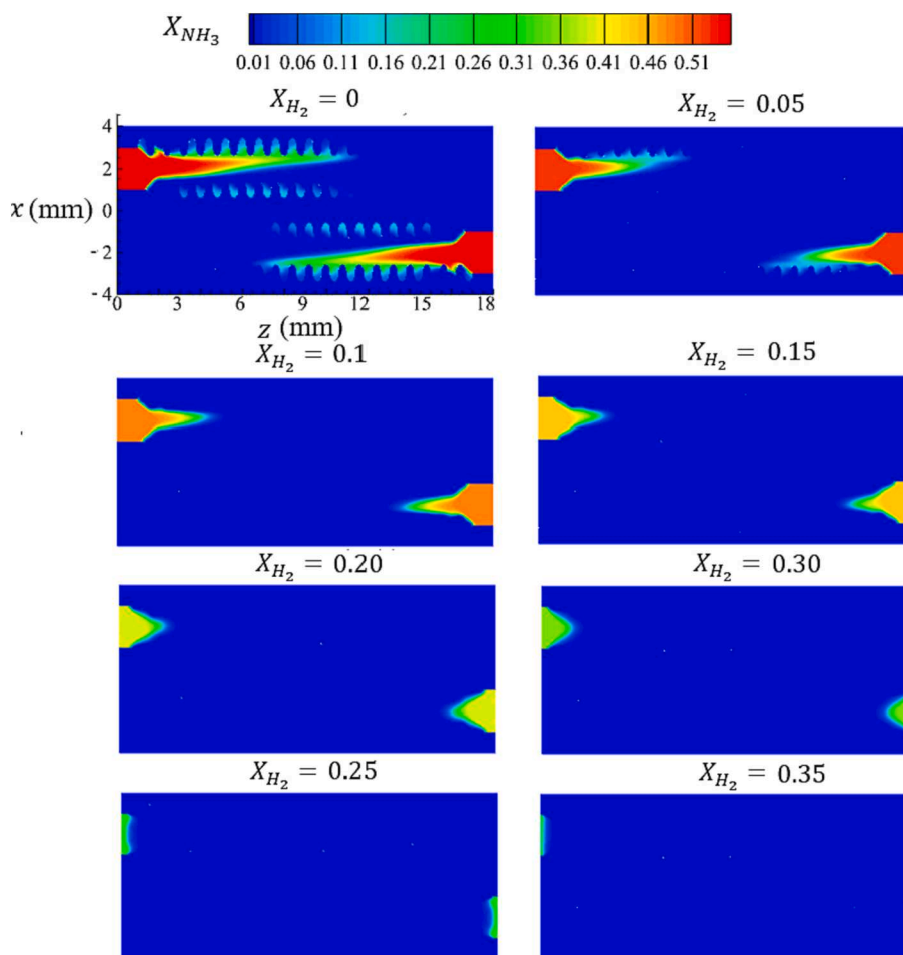
Fig. 16. Variation of the unburnt **NH₃** mole fraction in the counter-flow micro-combustors with the oval-shaped internal threads.
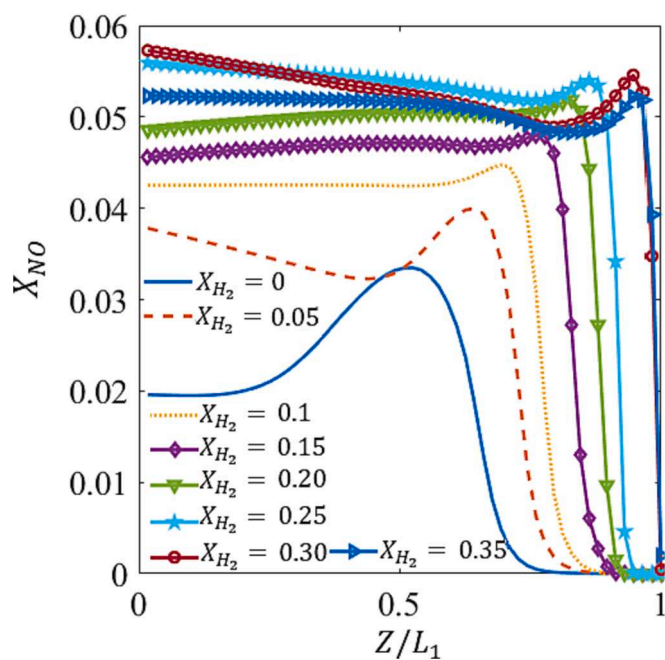

Fig. 17. Numerical predicted NO mole fraction along the centerline of different H_2 mole fraction at the inlet. Here, the inlet corresponds to dimensionless axial position $Z/L_1 = 1$.

by increasing Φ, while the changes of OH mole fraction peak result in the dramatic reduction of NO emission with increased Φ.

4. Further investigations on blending NH₃ with H₂

The micro-combustion stability may be dramatically improved by adding H_2 to the premixed fuel of NH_3/O_2 [56]. In this section, we explore the combustion properties and thermal performance by varying the H_2 mole fraction at the inlet (X_{H_2}). The H_2 mole fraction at the inlet is varied between 0 and 0.35. In all the following studies, the equivalence ratio Φ is set as 1, and the inlet velocity is 2 m/s.

As shown in Fig. 13, the peak of OH concentration increases with increasing the inlet H_2 mole fraction. This means that more H₂ blending in the inlet can stabilize the micro-combustion fuelled by ammonia. Furthermore, the area of OH concentration can be reduced. This could be explained by the greater burning speed that is associated with the addition of H₂. As mentioned above, the OH concentration can be utilized to determine the position of flame. It is clear that the position of the premixed flame has moved upstream by increasing the H₂ mole fraction. When the value of H₂ mole fraction at the inlet $X_{H_2} \geq 0.1$, the position of the flame tends to stabilize, associated with the reduced residence time of burning ammonia having a negative impact on chemical reactions. As X_{H_2} is varied from 0 to 3.5, the OH concentration is enhanced first and then decreased, reaching its highest at $X_{H_2} = 0.30$. Our results indicate that blending hydrogen in ammonia is beneficial to strengthen the chemical reaction of burning ammonia.

Fig. 14 shows the results of OH concentration on the micro-combustion. The position of the maximum temperature to the inlet is

Table 8
NO mole fraction at outlet under different H_2 mole fraction at the combustor inlet.

X_{H_2}	0	0.05	0.1	0.15	0.2	0.25	0.3	0.35
NO	0.0199	0.0387	0.0415	0.0451	0.048	0.0562	0.0582	0.0524

reduced by raising the inlet X_{H_2}. It shows that blending hydrogen with ammonia can increase the laminar burning speed of ammonia, which contributes to stabilizing the micro-combustion fuelled by ammonia evidently, which stabilizes the micro-combustion fuelled by ammonia and prevents the phenomenon of blow off in the micro-combustion fuelled by ammonia.

Fig. 15 illustrates flame temperature along the centerline of different H_2 mole fraction at the inlet. With the H_2 mole fractions ranging from 0 to 0.3, the highest temperature tends to increase with increases of X_{H_2}. Beyond $X_{H_2} = 0.3$, the maximum temperature starts to decrease. Meanwhile, the main reaction area to the inlet is reduced by increasing the inlet X_{H_2}. However, the temperature profile of $X_{H_2} = 0.3$ is very close to that of $X_{H2} = 0.35$, which means $X_{H_2} = 0.3$ is the best choice to improve the burning velocity of ammonia. The present results show that blending H_2 at the inlet can increase the burning velocity of ammonia and that $X_{H_2} = 0.3$ is the best choice to obtain the highest temperature in the fluid field.

Table 7 presents the MWT and the SDWT of different H_2 mole fraction at the inlet. From X_{H_2} in the range 0 to 0.25, the MWT increases with increased H_2. Meanwhile, the MWT reaches its highest at $X_{H_2} = 0.25$. Beyond $X_{H_2} = 0.25$, the MWT decreases with increasing X_{H2}. The SDWT shows to be uneven as increasing X_{H_2}. The results indicate that the MWT is negligibly influenced by the X_{H_2} and that the uniformity of the wall temperature is negatively influenced by the increase of the inlet mole fraction of H2. While the $X_{H_2} > 0.2$. It is obvious that blending hydrogen with the ammonia can move the highest temperature upstream, which intensifies the uneven wall temperature distribution. Again, it should be noted that while the MWT is influenced by X_{H2} these variations are small (less than 3%) and that the coefficient of variance (normalized standard deviation) is below 0.025 for all cases studied.

Fig. 16 illustrates the variation of the unburnt NH_3 mole fraction. It can be seen that the area of unburnt NH_3 can be reduced to the inlet as increasing X_{H_2}, which is caused by that the H_2 can strength the reaction of burning ammonia.

Fig. 17 illustrates the NO mole fraction along the centerline of different inlet H_2 mole fractions. The contours indicate that the X_{NO} experience steep increases near the inlet and these increases correspond to the regions of combustion. The NO mole fractions increases until they reach a local maximum and then gradually decrease. The location of inflection is nearer to the inlet for the cases with higher X_{H_2}. The results presented here indicate that adding H_2 into the inlet increases the production of NO dramatically at low values of H_2 and that this effect becomes less pronounced above $X_{H_2} = 0.2$. As the H_2 mole fraction is increased above $X_{H_2} = 0.3$, the production of NO is found to decrease, caused by that the highest temperature in the fluid field of $X_{H_2} = 0.3$ is higher than that of $X_{H_2} = 0.35$.

Table 8 shows the emissions of the micro-combustor affected by adding H2. It is worth noting that adding H_2 can cause an increase in *NO* emission. Especially, when $X_{H_2} = 0.05$ at the inlet, the growth of NO emission is almost double compared to $X_{H_2} = 0$. Beyond $X_{H_2} = 0.05$, the NO emission rises steadily though the growth rate tends to decrease. Furthermore, when $X_{H_2} = 0.30$, the NO mole fraction at the outlet reaches its peak, caused by excessive X_{H_2} that has a negative impact on the chemical reaction of NH_3/O_2. Results indicate that adding more H2 can result in an increase of NO emission, and NO emission target its highest at $X_{H_2} = 0.30$. From the current simulation. It is evident that adding hydrogen can cause an increase in the highest temperature. It is established that the increased temperature leads to more NO emission [51–55]. As X_{H_2} is varied from 0 to 0.15, the *OH* mole fraction is observed to be maximized, and the NO emission is increased. In other words, as more H_2 is added in the inlet, OH attends to improve the formation of ON. Since the growth rate of OH mole fraction peak starts to decrease as increasing X_{H_2} with X_{H_2} in the range 0.15 and 3.0, the NO emission shows the trend of tending to the same level as increasing X_{H_2}. This could be due to the fact that the improvement of the burning speed of ammonia is limited by adding H_2 in the range of $X_{H_2} = 0.15–3.0$.

5. Conclusions

In this work, a double-channel micro combustor with oval-shaped internal threads is employed to examine the thermal performance and NO emission fuelled by premixed ammonia/hydrogen/oxygen. The effects of the inlet velocity v_{in}, equivalence ratio ϕ and hydrogen mole fraction are examined. The key findings are listed below:

(1) the highest temperature is increased by increasing inlet velocity. Meanwhile, increasing the inlet velocity can cause the premixed flame and the highest temperature to migrate downstream, leading to an increase in mean wall temperature and a decrease in wall temperature uniformity. Furthermore, the NO emission at inlet velocity $v_{in} = 2$ m/s is the highest compared to other tested inlet velocity.

(2) The flame position is nearly independent of varying the equivalence ratio, when the equivalence ratio ≤ 1. As the equivalence ratio increased 1, the flame position shifts downstream, and the flame tends to be unstable. Moreover, the closer the equivalence ratio ϕ is to 1, the higher the mean wall temperature is. Additionally, increasing the equivalence ratio ϕ can cause an increase in the standard deviation of the wall temperature and NO emission.

(3) Increasing the inlet H_2 mole fraction can move the flame position to the inlet and intensify the chemical reaction of NH_3/O_2. However, the mean wall temperature does not get affected by blending H_2 with NH_3, evidently. On the contrary, the uniformity of the wall temperature is reduced by elevating the H_2 mole fraction at the combustor inlet. Moreover, blending the H_2 at the inlet can cause an increase in NO emission, and the NO emission reaches its highest under the H_2 mole fraction at the inlet is 0.3.

CRediT authorship contribution statement

He Zhao: Data curation, Investigation, Methodology, Software, Writing - original draft. **Dan Zhao:** Conceptualization, Funding acquisition, Investigation, Methodology, Project administration, Resources, Software, Supervision, Validation, Writing - original draft, Writing - review & editing. **Sid Becker:** Investigation, Writing - original draft, Writing - review & editing. **Yang Zhang:** Investigation, Writing - original draft, Writing - review & editing.

Declaration of Competing Interest

The authors declare that they have no known competing financial interests or personal relationships that could have appeared to influence the work reported in this paper.

Data availability

Data will be made available on request.

References

[1] Fan X, Liu C, Xu G, Zhang C, Wang J, Lin Y. Experimental investigations of the spray structure and interactions between sectors of a double-swirl low-emission combustor. Chin J Aeronaut 2020;33(2):589–97.

[2] https://unfccc.int/process-and-meetings/the-paris-agreement/the-paris-agreement.

[3] Li J, Huang H, Kobayashi N, He Z, Nagai Y. Study on using hydrogen and ammonia as fuels: Combustion characteristics and NOx formation. Int J Energy Res 2014;38:1214–23.

[4] Cai T, Zhao D. Enhancing and assessing ammonia-air combustion performance by blending with dimethyl ether. Renew Sustain Energy Rev 2022;156:112003.

[5] Zamfirescu C, Dincer I. Ammonia as a green fuel and hydrogen source for vehicular applications. Fuel Process Technol 2009;90(5):729–37.

[6] Zamfirescu C, Dincer I. Using ammonia as a sustainable fuel. J Power Sources 2008;185(1):459–65.

[7] Modak JM. Haber process for ammonia synthesis. Resonance 2011;16(12):1159–67.

[8] Frigo S, Gentili R. Analysis of the behaviour of a 4-stroke Si engine fuelled with ammonia and hydrogen. Int J Hydrogen Energy 2013;38(3):1607–15.

[9] Mathieu O, Petersen EL. Experimental and modeling study on the high-temperature oxidation of Ammonia and related NOx chemistry. Combust Flame 2015;162(3):554–70.

[10] Li J, Huang H, Kobayashi N, Wang C, Yuan H. Numerical study on laminar burning velocity and ignition delay time of ammonia flame with hydrogen addition. Energy 2017;126:796–809.

[11] Kailos NC. UTILIZATION OF AMMONIA AS AN ALTERNATE FUEL IN ARMY AIRCRAFT ENGINES. 1966.

[12] Boretti AA. Novel heavy duty engine concept for operation dual fuel H2–NH3. Int J Hydrogen Energy 2012;37(9):7869–76.

[13] Boretti A. Novel dual fuel diesel-ammonia combustion system in advanced TDI engines. Int J Hydrogen Energy 2017;42(10):7071–6.

[14] Mørch CS, Bjerre A, Gøttrup MP, Sorenson SC, Schramm J. Ammonia/hydrogen mixtures in an SI-engine: Engine performance and analysis of a proposed fuel system. Fuel 2011;90(2):854–64.

[15] Ryu K, Zacharakis-Jutz GE, Kong S-C. Effects of gaseous ammonia direct injection on performance characteristics of a spark-ignition engine. Appl Energy 2014;116:206–15.

[16] Kurata O, Iki N, Matsunuma T, Inoue T, Tsujimura T, Furutani H, et al. Performances and emission characteristics of NH3–air and NH3CH4–air combustion gas-turbine power generations. Proc Combust Inst 2017;36(3):3351–9.

[17] Dai L, Gersen S, Glarborg P, Levinsky H, Mokhov A. Experimental and numerical analysis of the autoignition behavior of NH3 and NH3/H2 mixtures at high pressure. Combust Flame 2020;215:134.

[18] Honzawa T, Kai R, Okada A, Valera-Medina A, Bowen PJ, Kurose R. Predictions of NO and CO emissions in ammonia/methane/air combustion by LES using a non-adiabatic flamelet generated manifold. Energy 2019;186:115771.

[19] Pugh D, Bowen P, Valera-Medina A, Giles A, Runyon J, Marsh R. Influence of steam addition and elevated ambient conditions on NOx reduction in a staged premixed swirling NH3/H2 flame. Proc Combust Inst 2019;37(4):5401–9.

[20] Reiter AJ, Kong S-C. Combustion and emissions characteristics of compression-ignition engine using dual ammonia-diesel fuel. Fuel 2011;90(1):87–97.

[21] Somarathne KDKA, Colson S, Hayakawa A, Kobayashi H. Modelling of ammonia/air non-premixed turbulent swirling flames in a gas turbine-like combustor at various pressures. Combust Theor Model 2018;22:973–97.

[22] Okafor EC, Somarathne KDKA, Hayakawa A, Kudo T, Kurata O, Iki N, et al. Towards the development of an efficient low-NOx ammonia combustor for a micro gas turbine. Proc Combust Inst 2019;37(4):4597–606.

[23] Konnov AA. Implementation of the NCN pathway of prompt-NO formation in the detailed reaction mechanism. Combust Flame 2009;156(11):2093–105.

[24] Duynslaegher C, Contino F, Vandooren J, Jeanmart H. Modeling of ammonia combustion at low pressure. Combust Flame 2012;159(9):2799–805.

[25] Okafor EC, Naito Y, Colson S, Ichikawa A, Kudo T, Hayakawa A, et al. Measurement and modelling of the laminar burning velocity of methane-ammonia-air flames at high pressures using a reduced reaction mechanism. Combust Flame 2019;204:162–75.

[26] Xiao H, Valera-Medina A, Bowen PJ. Modeling Combustion of Ammonia/Hydrogen Fuel Blends under Gas Turbine Conditions. Energy Fuel 2017;31:8631–42.

[27] Meng X, Zhang M, Zhao C, Tian H, Tian J, Long W, et al. Study of combustion and NO chemical reaction mechanism in ammonia blended with DME. Fuel 2022;319:123832.

[28] Sun Y, Cai T, Shahsavari M, Sun D, Sun X, Zhao D, et al. RANS simulations on combustion and emission characteristics of a premixed NH3/H2 swirling flame with reduced chemical kinetic model. Chin J Aeronaut 2021;34(12):17–27.

[29] Liukkonen M, Heikkinen M, Hiltunen T, Halikka E, Kuivalainen R, Yrjö H. Modeling of Process States by Using Artificial Neural Networks in a Fluidized Bed Energy Plant. 2009.

[30] Krzywanski J, Blaszczuk A, Czakiert T, Rajczyk R, Nowak W. Artificial intelligence treatment of NOx emissions from CFBC in air and oxy-fuel conditions. 2014.

[31] Krzywanski J, Czakiert T, Nowak W, Shimizu T, Zylka A, Idziak K, et al. Gaseous emissions from advanced CLC and oxyfuel fluidized bed combustion of coal and biomass in a complex geometry facility: A comprehensive model. Energy 2022;251.

[32] Krzywanski J, Czakiert T, Zylka A, Nowak W, Sosnowski M, Grabowska K, et al. Modelling of SO2 and NOx Emissions from Coal and Biomass Combustion in Air-Firing, Oxyfuel, iG-CLC, and CLOU Conditions by Fuzzy Logic Approach. Energies 2022;15(21).

[33] Iki N, Kurata O, Matsunuma T, Inoue T, Suzuki M, Tsujimura T, et al. Micro Gas Turbine Firing Kerosene and Ammonia. *ASME Turbo Expo 2015: Turbine Technical Conference and Exposition.* Volume 8: Microturbines, Turbochargers and Small Turbomachines; Steam Turbines. 2015.

[34] Nakamura H, Hasegawa S, Tezuka T. Kinetic modeling of ammonia/air weak flames in a micro flow reactor with a controlled temperature profile. Combust Flame 2017;185:16–27.

[35] Okafor EC, Somarathne KDKA, Ratthanan R, Hayakawa A, Kudo T, Kurata O, et al. Control of NOx and other emissions in micro gas turbine combustors fuelled with mixtures of methane and ammonia. Combust Flame 2020;211:406–16.

[36] Cai T, Zhao D, Wang B, Li J, Guan Y. NOx emission and thermal performances studies on premixed ammonia-oxygen combustion in a CO2-free micro-planar combustor. Fuel 2020;280:118554.

[37] Yan Y, Tang W, Zhang L, Pan W, Li L. Thermal and chemical effects of hydrogen addition on catalytic micro-combustion of methane–air. Int J Hydrogen Energy 2014;39(33):19204–11.

[38] Shih H-Y, Liu C-R. A computational study on the combustion of hydrogen/methane blended fuels for a micro gas turbines. Int J Hydrogen Energy 2014;39(27):15103–15.

[39] Yan Y, Wang H, Pan W, Zhang L, Li L, Yang Z, et al. Numerical study of effect of wall parameters on catalytic combustion characteristics of CH4/air in a heat recirculation micro-combustor. Energ Conver Manage 2016;118:474–84.

[40] Li Y-H, Chen G-B, Hsu H-W, Chao Y-C. Enhancement of methane combustion in microchannels: Effects of catalyst segmentation and cavities. Chem Eng J 2010;160(2):715–22.

[41] Chen J, Song W, Xu D. Optimal combustor dimensions for the catalytic combustion of methane-air mixtures in micro-channels. Energ Conver Manage 2017;134:197–207.

[42] Wan J, Fan A, Maruta K, Yao H, Liu W. Experimental and numerical investigation on combustion characteristics of premixed hydrogen/air flame in a micro-combustor with a bluff body. Int J Hydrogen Energy 2012;37(24):19190–7.

[43] Wei J, Peng Q, Shi Z, Xie B, Kang Z, Ye J, et al. Investigation on the H2 fueled combustion with CH4 and C3H8 blending in a micro tube with/without fins. Fuel 2022;328:125314.

[44] Li Q, Li J, Shi J, Guo Z. Effects of heat transfer on flame stability limits in a planar micro-combustor partially filled with porous medium. Proc Combust Inst 2019;37(4):5645–54.

[45] Wan J, Fan A, Yao H. Effect of the length of a plate flame holder on flame blowout limit in a micro-combustor with preheating channels. Combust Flame 2016;170:53–62.

[46] Zhang Z, Shen W, Yao W, Wang Q, Zhao W. Effect of helical fins on the combustion performance in a micro-step combustor. Fuel 2022;319:123718.

[47] Su Y, Song J, Chai J, Cheng Q, Luo Z, Lou C, et al. Numerical investigation of a novel micro combustor with double-cavity for micro-thermophotovoltaic system. Energ Conver Manage 2015;106:173–80.

[48] Zhao H, Zhao D, Becker S. Entropy production and enhanced thermal performance studies on counter-flow double-channel hydrogen/ammonia-fuelled micro-combustors with different shaped internal threads. Int J Hydrogen Energy 2022;47(85):36306–22.

[49] Zuo W, E J, Peng Q, Zhao X, Zhang Z. Numerical investigations on thermal performance of a micro-cylindrical combustor with gradually reduced wall thickness. Applied Thermal Engineering 2017;113:1011-20.

[50] Ni S, Zhao D, Zhu X. Heat transfer and entropy production evaluation on premixed hydrogen/air-fuelled micro-combustors with internal threads. Fuel 2021;303:121325.

[51] Han X, Wang Z, Costa M, Sun Z, He Y, Cen K. Experimental and kinetic modeling study of laminar burning velocities of NH3/air, NH3/H2/air, NH3/CO/air and NH3/CH4/air premixed flames. Combust Flame 2019;206:214–26.

[52] Okafor EC, Naito Y, Colson S, Ichikawa A, Kudo T, Hayakawa A, et al. Measurement and modelling of the laminar burning velocity of methane-ammonia-air flames at high pressures using a reduced reaction mechanism. Combustion and Flame 2019;204(JUN.):162-75.

[53] Shen Z, Yang D, Li Y, Liang Z, Wan L. Numerical analysis of heat transfer to water flowing in rifled tubes at supercritical pressures. Appl Therm Eng 2018;133:704–12.

[54] Stelzner B, Keramiotis C, Voss S, Founti MA, Trimis D. Analysis of the flame structure for lean methane–air combustion in porous inert media by resolving the hydroxyl radical. Proc Combust Inst 2015;35(3):3381–8.

[55] Glarborg P, Miller JA, Ruscic B, Klippenstein SJ. Modeling nitrogen chemistry in combustion. Prog Energy Combust Sci 2018;67:31–68.

[56] Sun Y, Cai T, Shahsavari M, Sun D, Wang B. RANS simulations on combustion and emission characteristics of a premixed NH3/H2 swirling flame with reduced chemical kinetic model. Chin J Aeronaut 2021.